



HAL
open science

A new methodology inspired from the Theory of Critical Distances for determination of inherent tensile strength and fracture toughness of rock materials

S. Aligholi, Laurent Ponson, Q.B. Zhang, A.R. Torabi

► To cite this version:

S. Aligholi, Laurent Ponson, Q.B. Zhang, A.R. Torabi. A new methodology inspired from the Theory of Critical Distances for determination of inherent tensile strength and fracture toughness of rock materials. *International Journal of Rock Mechanics and Mining Sciences*, 2022, 152, pp.105073. 10.1016/j.ijrmms.2022.105073 . hal-03974124

HAL Id: hal-03974124

<https://hal.sorbonne-universite.fr/hal-03974124>

Submitted on 5 Feb 2023

HAL is a multi-disciplinary open access archive for the deposit and dissemination of scientific research documents, whether they are published or not. The documents may come from teaching and research institutions in France or abroad, or from public or private research centers.

L'archive ouverte pluridisciplinaire **HAL**, est destinée au dépôt et à la diffusion de documents scientifiques de niveau recherche, publiés ou non, émanant des établissements d'enseignement et de recherche français ou étrangers, des laboratoires publics ou privés.

1

2 **A new methodology inspired from the theory of critical distances for determination** 3 **of inherent tensile strength and fracture toughness of rock materials**

4

5 **S. Aligholi^{a,*}, L. Ponson^b, A.R. Torabi^c, Q.B. Zhang^a**

6

^a*Department of Civil Engineering, Monash University, VIC 3800, Australia*

7

^b*Fracture Lab, Institut Jean le Rond d'Alembert, CNRS – Sorbonne Université, Paris, France*

8

^c*Fracture Research Laboratory, Faculty of New Science and Technologies, University of Tehran, Tehran, Iran*

9

10 **Abstract**

11 Measuring the intrinsic fracture properties of quasi-brittle materials like rocks is of great importance and
12 at the same time a major issue for engineers. In this study, we explore the ability of the Theory of Critical
13 Distances (TCD) to determine accurately both the tensile strength and the fracture toughness. To this end, we
14 conduct ring tests and semi-circular bend tests on four rock types including a red sandstone, a white coarse-
15 grained marble, a fine-grained granite and a coarse-grained granite. This selection covers sedimentary,
16 metamorphic and igneous rock types with different grain sizes. The experimental data are analysed using a new
17 methodology developed from the so-called Point Method (PM), a particular form of the TCD, from which we
18 infer the intrinsic tensile strength and the fracture toughness of the studied rock materials. Our results are
19 compared with those obtained from the methodology recommended by ISRM that is modified to take into
20 account the finite notch root radius used in our experiments. The comparison is successful, supporting that the
21 newly developed methodology is suitable to determine the intrinsic tensile strength and the fracture toughness
22 of rock materials.

23

24 **Keywords:** Critical distance, Intrinsic tensile strength, Fracture toughness, Point method, Notch mechanics

25

* Corresponding Author:

E-mail address: aligholisaeed1@gmail.com ; saeed.aligholi@monash.edu

26 1. Introduction

27 Rocks are archetypes of quasi-brittle materials. Under compression, they generally show a rather extended
28 non-linear regime owing to the spreading of micro-fractures before final failure takes place. Under traction, they
29 fail through the propagation of a crack that grows through the coalescence of micro-cracks localized at the crack
30 tip vicinity in the so-called process zone. If the spatial extent of the process zone is small with respect to the
31 specimen size, this phenomenon is then appropriately described by the theory of Linear Elastic Fracture
32 Mechanics (LEFM).¹ Within the LEFM framework, we introduce the fracture toughness K_{Ic} that quantifies the
33 ability of the material to resist to crack growth. Alternatively, one can seek to determine the stress level at which
34 the material fails in traction, thus defining the material tensile strength. This is of particular relevance in absence
35 of an initial crack in the structure.^{2,3} However, defining an intrinsic (specimen independent) tensile strength for
36 quasi-brittle solids is a rather difficult challenge, as the load-bearing capacity of quasi-brittle specimens is
37 known to strongly depend on its size,^{4,5} and often overlooked in engineering practice.⁶

38 Owing to their quasi-brittle nature, rock made structures can give rise to catastrophic failures. Therefore,
39 the accurate determination of their failure properties is key to assess the structural resistance of rock masses, an
40 important issue in many rock engineering practices such as tunnelling, rock cutting processes, hydraulic
41 fracturing and rock slope stability.⁷ In the following, the term *structural* properties is used when the geometrical
42 features of the specimens or bodies do play a significant role on top of the *intrinsic* properties that depend only
43 on the microstructural features of the rock materials as well as the surrounding environment.⁸

44 A suitable solution for defining the tensile strength of rocks consists in considering the characteristic stress
45 level at which the material fails within the process zone of a stress concentrator or a running crack. According
46 to the Cohesive Zone Model (CZM) for brittle cracks,⁹⁻¹⁰ the so-called cohesive strength σ_c of the material is
47 then related to the material fracture toughness via the cohesive length ℓ_c (or process zone size along the crack
48 propagation direction) through the relation $K_{Ic} \propto \sigma_c \sqrt{\ell_c}$.⁹ Although appealing, this definition raises serious
49 experimental issues: how to determine the stress level at the tip of stress concentrators, as the process zone is
50 hardly larger than 1 mm in most quasi-brittle specimens.

51 Theoretically speaking, specimens without stress concentrator could be tested under direct tension to
52 determine the material tensile strength while specimens with sharp cracks can be used to measure the material
53 fracture toughness. However, in practice, such a procedure is neither reliably achievable nor practical. On the
54 one hand, it turns out that specimens without stress concentrators cannot be used to determine the tensile strength
55 of rock materials. The reasons behind this observation have been largely discussed by researchers e.g. 4, 11 and
56 relates to the stochastic (defect driven) nature of tensile failure. On the other hand, preparing sharp cracks in
57 rock specimens is a challenging task.

58 Considering these issues, new methodologies based on different concepts have been proposed to reliably
59 determine the tensile strength and fracture toughness of different materials including rocks. One of them is the
60 so-called Theory of Critical Distances (TCD) based on notch mechanics. It aims at providing simple and
61 practical tools to engineers including rock engineers. TCD includes a group of theories used for predicting the
62 effects of stress concentrators on material behaviour under mechanical loads.¹² The TCD can take different
63 forms and has been used with success in a wide range of engineering problems to determine or predict properties
64 of different materials including composites,¹³⁻¹⁴ metals,¹⁵⁻¹⁷ polymers,¹⁸⁻¹⁹ and rocks.²⁰⁻²³ The TCD can
65 circumvent the experimental difficulties encountered when it comes to determining the intrinsic tensile strength
66 and fracture toughness of quasi-brittle materials. With such an approach, specimens without stress concentrators
67 or perfectly sharp cracks are not required to determine these properties, as we will show in the following.
68 Furthermore, notch mechanics can be applied to modify the effect of a round-tip notch on apparent fracture
69 toughness of materials and provide engineers with accurate values of fracture toughness,²⁴⁻²⁷ as also detailed
70 later.

71 This paper is organized as follows. First, we present the studied rock materials as well as the experimental
72 and analytical methods adopted for this study. A brief theoretical background on the methodology employed to
73 analyse the ring tests and bending tests carried in this study is provided in Section 2. Section 3 presents our main
74 results including a discussion. Finally, the conclusions of our study are drawn in Section 4.

75

76 **2. Materials and Methods**

77 Four different rock types including a red sandstone, a white coarse-grained marble, a fine-grained granite
78 and a coarse-grained granite are selected for this study. This selection covers sedimentary, metamorphic and
79 igneous rock types with different grain sizes. The PM form of the TCD is applied to measure accurately the
80 failure properties of these rock materials including tensile strength and fracture toughness. To check the validity
81 of the proposed PM, the fracture toughness of the tested rocks is also measured according to the ISRM Suggested
82 Method²⁸ modified to take into account the finite radius of the notch used in our experiments.

83

84 **2.1. A modified version of the PM based on CZM**

85 The PM is the simplest form of the TCD.²⁹ Its failure criterion has been defined by Taylor³⁰ as follows:
86 ‘Failure will occur when the stress at a distance $L/2$ from the notch root is equal to σ_0 ’. This translates as:

$$\sigma(L/2) = \sigma_0 \quad (1)$$

87 where L is a characteristic distance, and σ_0 is the inherent tensile strength of the material. If the stress distribution
 88 ahead of a stress concentrator and the characteristic distance are known, then the inherent tensile strength can
 89 be determined. As justified in Appendix A, the material fracture toughness K_{Ic} can finally be estimated from
 90 the relation:

$$L = \frac{1}{\pi} \left(\frac{K_{Ic}}{\sigma_0} \right)^2 \quad (2)$$

91 Although the PM has been successfully applied to a large range of fracture problems, it remains a
 92 phenomenological method.³⁰ Interestingly, it is intimately connected to the CZM of failure, which rigorously
 93 extends LEFM to elasto-damageable solids. In its simplest version, CZM introduces a cohesive stress σ_c , below
 94 which the material behaves elastically and beyond which it does not sustain any mechanical load. This approach
 95 predicts the spatial extent of the fracture process zone, also called the cohesive zone, through the Dugdale–
 96 Barenblatt (D–B) formula (see Appendix A):^{9,31}

$$\ell_c = \frac{\pi}{8} \left(\frac{K_{Ic}}{\sigma_c} \right)^2 \quad (3)$$

97 This formula is almost identical to Eq. (2) up to a constant $\pi^2/8 \approx 1.23$. On top of it, considering the tensile
 98 stress distribution $\sigma(r) = K_I/\sqrt{2\pi r}$ ahead of a running crack as predicted by LEFM, one infers the relation
 99 $\sigma(4\ell_c/\pi^2) = \sigma_c$ that is similar to Eq. (1). In the following, we use Eq. (3) instead of Eq. (2), as it derives from
 100 a well-identified assumption, namely the existence of a unique stress level that provides both the elastic limit
 101 and the failure threshold of the material, but we use the following PM based methodology to determine both σ_c
 102 and ℓ_c .

103 Specimens with different notch geometries are loaded up to failure. Following Eq. (1), the point of
 104 intersection of the stress distribution ahead of the stress concentrators at the onset of failure is expected to
 105 provide the material tensile strength. Following the previous interpretation of the PM based on CZM, two
 106 extreme stress concentrators, i.e. a sharp notch (very high-stress concentration) and a flat free surface (no stress
 107 concentration), are best suited. However, in practice, machining very sharp notches and initiating a crack from
 108 a flat free surface are quite difficult to achieve in rock materials.

109 To circumvent these difficulties, Semi-Circular Bend (SCB) specimens with a notch root radius of about
 110 350 μ m and ring specimens with an inner radius of around 14mm are used to produce the highest and lowest
 111 possible stress concentrations, respectively. Despite the discrepancy between these specimens and the perfect

112 concentrators expected theoretically, our method provides accurate values of tensile strength, as we will show
113 in Section 3.

114

115 2.2. Ring test

116 Rock rings are used in the following as the low-stress concentrator specimens. This test geometry has been
117 used in the past to measure the apparent tensile strength of rocks and other brittle materials.^{32,33} Note however
118 the apparent tensile strength is a structure-dependent property rather than an inherent material property.^{11,34} The
119 difference between the value of the apparent tensile strength and σ_c results from the combination of three
120 factors: (1) the probabilistic nature of the resistance of materials to tensile loading; (2) the complexity of the
121 failure process involving the initiation of a crack by damage accumulation before it can propagate; and (3) the
122 calculated stress following a linear elastic assumption may not be the 'real' stress experienced by the material.¹¹

123 The minimum diameter of the internal hole that could be drilled into the sandstone and the marble is about
124 3mm, while it is about 6mm for granites (Fig. 1-c). Rings with four different inner diameters are prepared for
125 the sandstone and the marble, whereas three different ring specimens are prepared for granites. Moreover,
126 normal disk specimens with no hole are also prepared and tested for all rock types. At least three different
127 specimens for any geometry are tested and the average of calculated tensile strengths for each rock
128 type/geometry is used for further analyses. The outer diameter and thickness of the rings/disks are around 75
129 and 30 mm, respectively. Note that, following the analysis of Fillon,³⁵ the ratio of the inner to the outer diameter
130 of our ring specimens is less than or equal to 0.4 so that the tensile mode of failure dominates over the
131 compressive one.³² The driving rate of the cross-head for all our tests is set to 0.05 mm/min.

132 The apparent tensile strength σ_{\max} is defined as the maximum stress level applied locally to the material at
133 the onset of failure, assuming that it behaves elastically everywhere. It then follows:

$$\sigma_{\max} = \frac{P_{\max}}{\pi B R_0} [6 + 38(R/R_0)^2] \quad (4)$$

134 that provides the tensile stress applied to the inner surface of the specimen at the applied failure load P_{\max} . For
135 disk specimens for which $R = 0$, the maximum applied stress is located at the center of the specimen and
136 follows:

$$\sigma_{\max} = \frac{P_{\max}}{\pi B R_0} \quad (5)$$

137 Here, B is the ring thickness while R and R_0 are the inner and outer radii of the ring, respectively.

138 Following Torabi et al.,³⁶ Kirsch's solution together with Hobbs' correction³² are used to determine the
139 tensile stress distribution $\sigma_x(y)$ along the loading axis y (see the schematic of the ring specimen shown in Fig.
140 1-a for the definition of the axes x and y):

$$\sigma_x(y) = \frac{\sigma_{\max}}{2} \left(2 - 2 \frac{R^2}{y^2} + 12 \frac{R^4}{y^4} \right) F_{\text{corr}} \quad (6)$$

141 Here, F_{corr} is a correction factor that should be taken into account for sufficiently large R/R_0 ratios, which
142 follows:

$$F_{\text{corr}} = 1 + \frac{19}{3} \left(\frac{R}{R_0} \right)^2. \quad (7)$$

143 In the course of the ring experiments, we observe an interesting phenomenon that we would like to discuss.
144 As shown in Figs. 2-b and 2-d, the mechanical response of the ring specimen with the largest inner radius shows
145 two peaks, the first one being larger than the second one. It turns out that full failure of the ring specimen took
146 place in two steps. First, as the load is increased, the tensile strength of the material is reached and failure takes
147 place at point A (see Fig. 2-c). After stress drop, the sample is still able to sustain load. As a result, the applied
148 load increases again, starting from a lower level until it reaches a second time the tensile strength of the material
149 at point C (see Fig. 2-c). It is interesting to notice that each half of the sample can still bear some compressive
150 load until the tensile strength of the material is reached a second time at point C, and providing a good evidence
151 that the sample has been split under pure tension at point A.

152 The first and second peaks in Fig. 2-d corresponds to the fractures labelled in Fig. 2-c and located at points
153 A and C, respectively. From this observation, it can be concluded that ring test is suitable to measure the tensile
154 strength. From recorded videos by high-speed cameras, we do observe that rings with smaller internal holes are
155 always separating from point A in a tensile mode as well (Fig. 3), as expected from direct numerical simulations
156 of failure in such specimens.³³

157

158 2.3. Semi-circular bending test

159 The notched semi-circular geometry is used for preparing rock specimens with high-stress concentrators.
160 Various methods have been used to determine the fracture toughness of rock materials.^{e.g. 28,37-39} The method

161 suggested by ISRM ²⁸ relies on SCB specimens that is rather simple to machine and provides good
162 repeatability.^{e.g. 40-43}

163 Herein, SCB specimens are prepared and tested according to ISRM. Multiple SCB specimens for each rock
164 type are tested and the average generalized (or apparent) fracture toughness K_{Ic}^U is calculated as follows:

$$K_{Ic}^U = Y' \frac{P_{max} \sqrt{\pi a}}{DB} \quad (8)$$

165 Here a , B , D , and P_{max} are the notch length, the specimen thickness, the diameter of the SCB specimen and the
166 maximum applied load, respectively (see Fig. 4). The notch length of the tested SCB specimens is comprised
167 between 14 to 16 mm while the notch tip radius is 350 microns. The diameter and the thickness of the SCB
168 specimens range from 74 to 76 mm and 29 to 31 mm, respectively. Finally, Y' gives the non-dimensional stress
169 intensity factor derived using the finite element method while assuming plane-strain conditions.²⁸ Its expression
170 follows:

$$Y' = -1.297 + 9.516(s/D) - (0.47 + 16.457(s/D))\beta + (1.071 + 34.401(s/D))\beta^2 \quad (9)$$

171 where s is the span length which is between 37 to 38 mm for all our tests while β is equal to $2a/D$.

172 Failure of SCB specimens is recorded by means of a high-speed camera (Fig 5-a). It can be clearly seen
173 that the fracture initiates from the notch tip and propagates parallel to the axis of application of the forces, as
174 expected. Typical load-extension curves obtained for different rock types are shown in Fig 5-b.

175 Creager–Paris solution ²⁴ provides the stress distribution in SCB specimens with a blunted notch of radius
176 ρ :

$$\sigma(x, 0) = \frac{2K^U}{\sqrt{\pi}} \frac{x + \rho}{(2x + \rho)^{3/2}} \quad (10)$$

177 using the coordinate system depicted in Fig. 4-b. K^U , the apparent stress intensity factor, is provided by Eq. (8)
178 after replacing the failure load P_{max} by the current applied load P .

179

180 2.4. Direct fracture toughness measurement using SCB tests

181 To test the ability of the proposed methodology to accurately measure the fracture toughness of rock
 182 materials, we proceed to an independent measurement of K_{IC} using the failure load of the semi-circular bending
 183 tests. The basic idea is to consider that at the onset of failure, the imposed stress intensity factor (determined
 184 from Eqs. (8) and (9) at the tip of the notch) reaches the fracture toughness value K_{IC} . However, in our
 185 experiments, the notch tip radius is too large to be neglected. Compiling a large set of experimental data, Gomez
 186 et al.²⁵ determined the ratio of the apparent fracture toughness (resulting from the finite notch root radius) over
 187 the actual material fracture toughness:

$$\frac{K_{IC}^U}{K_{IC}} = \sqrt{1 + \frac{\pi}{4} \frac{\rho}{(K_{IC}/\sigma_c)^2}} \quad (11)$$

188 Here, the intrinsic tensile strength σ_c is determined using the PM based methodology while ρ measured
 189 from 2D slices of SCB specimens scanned by means of X-ray tomography, is found to be close to 350 microns
 190 (Fig. 4-d). K_{IC}^U corresponds to the apparent fracture toughness measured experimentally. As the material fracture
 191 toughness K_{IC} appears on both sides of this equation, Eq. (11) must be solved iteratively following the procedure
 192 described in Appendix B and illustrated in Figs. 6-a and 6-b. It turns out that the ratio K_{IC}/K_{IC}^U is close to 0.95
 193 for the four materials investigated.

194 Beyond the particular cases of the fracture tests carried in this study, Figs. 6-c and 6-d depicts the effect of
 195 the cohesive length in comparison to the notch root radius on the ratio K_{IC}/K_{IC}^U . In particular, it can be seen that
 196 small notch radii compared to cohesive length give rise to $K_{IC} \approx K_{IC}^U$.

197

198 3. Results and discussion

199 3.1. Size effect on tensile strength measurements using ring specimens

200 A natural first step in assessing the structure-independent tensile strength of the rock materials investigated
 201 is to determine the apparent (structure dependent) tensile strength σ_{max} as a function of the ring geometry. Ring
 202 specimens with various inner radii as well as disk specimens from different rock types are tested for such a
 203 purpose. Fig. 7-a shows the value of σ_{max} as a function of the inner hole radius as obtained after averaging over
 204 different samples. It appears that the apparent tensile strength strongly depends on the hole radius (Fig. 7-b).
 205 This calls for a more advanced method of analysis to determine the inherent tensile strength.

206

207 3.2. Intrinsic tensile strength and material fracture toughness

208 The methodology described in Section 2.1 based on the SCB specimens with a notch root radius of 350
209 microns (high concentrator) and the ring specimens with inner radii of 13–15mm (low concentrator) is applied
210 in Fig. 8 for the four rocks investigated. According to Eq. (1), the intersection point of the tensile stress
211 distributions at the onset of failure for both ring and SCB specimens provides both the inherent tensile strength
212 and the cohesive zone length. The fracture toughness value is then obtained from Eq. (3) using the D–B
213 relationship. The results obtained for the four rocks investigated are summarized in Table 1.

214 The validity of the proposed methodology is now tested. First, we compare the fracture toughness value
215 predicted by Eq. (3) with the fracture toughness value measured directly from the notched SCB specimen, after
216 taking into account the effect of its finite notch root radius. For this purpose, the value of σ_c determined
217 previously is used in Eq. (11), providing the ratio K_{Ic}/K_{Ic}^U between the inherent fracture toughness and the
218 apparent one, as explained in Sec. 2.4. The comparison shown in Table 2 is excellent. We then compare in Table
219 3 the cohesive zone length as measured from our method using the intersection point between both stress
220 distributions at the onset of failure (see Fig. 8) with the one predicted from D–B Formula using the fracture
221 toughness determined directly from the notched SCB tests and modified for the rounded notch tip effect. Here
222 also, the agreement is very good. Last but not least, we did proceed to an independent measurement of the
223 process zone length from statistical fractography, a technique that consists in analysing the statistics of fracture
224 surface roughness to extract the characteristic size of the damage processes taking place at the crack tip vicinity
225 during propagation, and found values comparable to the one determined in this study, i.e. in the range 0.7 – 1
226 mm.

227 These results call for a few comments. First, the intrinsic tensile strength varies in the range 8 – 25 MPa
228 for the different rock materials investigated. This is somehow larger, however comparable to the values reported
229 in the literature for such materials.^{6,44} Note that using smaller hole radius for the low stress concentrator gives
230 larger values of σ_c , as inferred from Fig. 9 where the tensile stress distribution at the onset of failure is
231 represented for the different specimen geometries. First, considering stronger stress concentrator is not
232 compatible with the justification of Eq. (1) that requires the combination of a high and a low stress concentrator
233 (see Section 2.1). Second, it leads to smaller values of cohesive length, of the order of a few hundred of microns,
234 that do not match with the results inferred from the statistical analysis of the fracture surfaces.

235 We then would like to discuss the fracture toughness values measured for the four rocks investigated. Our
236 methodology provides accurate fracture toughness values, in agreement with values of K_{Ic} determined directly
237 from the notched SCB specimens using the ISRM suggested method. Afterwards, it turns out that the value of
238 the apparent fracture toughness obtained with a notch root radius less than 500 microns as suggested by ISRM
239 already provides a rather good estimate of K_{Ic} for the rocks investigated. Overall, precision achieved by both
240 methods is remarkable.

241

242 3.3. Discussion

243 So far, the results are interpreted and it is concluded that PM is successful in order to measuring intrinsic
244 tensile strength and material fracture toughness, especially when the D–B formula is being used to determine
245 the material fracture toughness. This conclusion can open new doors for future researches and needs further
246 enlightening. The main questions should be answered concerning these results are: 1) Why PM is successful?
247 2) Why D–B formula is giving better results?

248 To answer these fundamental questions, first, we need to give a brief background of PM, and both original
249 and developed methods used to calculate the characteristic length L . As discussed in section 2, Eq. (1) introduced
250 by Peterson⁴⁵ is the main failure criterion of PM. This formula is considering a material dependent characteristic
251 length inferring the estimated stress for a particular geometry at a distance $L/2$ from its concentrator is equal to
252 inherent tensile strength of the material. In this argument, L is a constant characteristic length depends on
253 intrinsic properties of a material, and is independent from geometry of specimen. Therefore, for homogeneous
254 materials, stress distribution, as a function of distance from concentrator, of any two different geometries would
255 intersect at a point showing material properties. The abscissa of this point is half of the material characteristic
256 length and its ordinate is intrinsic tensile strength.

257 Although PM is successful in practice, from above presentation, there are two major facts lacking
258 applicability and supportive theoretical arguments. First, materials are not homogeneous and there should be
259 always some rooms for experimental calibrations, even though one uses the highest and lowest possible stress
260 concentrators for determining the intersection point as it is done in this study. Second, how the L should be
261 determined to further estimate material fracture toughness and why $L/2$ is corresponding to material tensile
262 strength. The first issue concerning applicability of this model is out of scope of this study and will be addressed
263 in a future work. From the results of this study, the second issue turns out to be very important and can increase
264 the accuracy of PM with some modifications. Not solid, but it is reasonable to consider the stress at half of the
265 characteristic length L would be equal to intrinsic tensile strength. It is somehow representing the average stress
266 over L that lead to failure of material. It is notable that this argument is close to CZM assumptions for derivation
267 of Eq. 3 (refer to Appendix A).

268 Barenblatt⁹ and Dugdale³¹ separately and at the same time have developed basis for the CZM. Their
269 models have different theoretical arguments and physics but treat the problem with similar procedures.
270 Barenblatt model is looking at the problem at microscopic scale and considers inter-molecular cohesive stresses
271 at a large enough area for applying continuum fracture mechanics, and is suitable for brittle materials. Dugdale
272 model is a macroscopic model and considers perfectly plastic material behaviour inside the process zone ahead
273 of crack tip. In these models, the process zone (the cohesive zone in Barenblatt model or the plastic zone in
274 Dugdale model) in direction of applied load (y) is small compared to its length in crack propagation direction
275 (x). Moreover, in Barenblatt model the length of cohesive zone is small in comparison to crack length $\ell_c \ll a$,

276 and the distribution of cohesive stress σ_c in the cohesive zone for a given material is always the same and
277 independent of the external load.⁴⁶ These two models in the most simplified scenario (strip or line model) will
278 be end up with the same closed form solution, and this is why Eq. (3) referred to as D–B formula (refer to
279 Appendix A).

280 Overall, considering CZM and PM descriptions it makes sense to employ D–B formula instead of Eq. (2)
281 for calculating the characteristic length. On the one hand, PM asserts L is material dependent and can be
282 determined by testing specimens from same material but different geometries. On the other hand, Barenblatt
283 model argues distribution of σ_c in the cohesive zone for a given material is always the same and depends on
284 material properties. Finally, although these formulas considering different stress distributions over L or ℓ_c , both
285 Eq. (1) and Eq. (3) are considering average stress at $L/2$ at the moment of failure, and it seems D–B model
286 assumptions are closer to reality.

287

288 **4 Conclusions**

289 In this study, a TCD based methodology is examined to determine two key mechanical properties of rock
290 materials namely intrinsic tensile strength and material fracture toughness. The first and foremost conclusion is
291 that PM form of TCD is a suitable means to reliably determine intrinsic tensile strength and material fracture
292 toughness of different rock types. According to our results, PM is very reliable if the cohesive length ℓ_c is
293 considered as the characteristic length L in this method.

294 Following the results of this study, it turns out that plane disk specimens without stress concentrators cannot
295 be used to measure tensile strength of rock materials, and tensile strength is underestimated if plane specimens
296 are used. However, it could provide engineers with a safe and conservative estimation despite the fact that it
297 would often increase the costs of a project. From the observations in the course of ring experiments, it can be
298 concluded that ring test is a suitable means to measure apparent tensile strength of rock materials. Tensile
299 strength of rocks revealed to depend on their structural properties due to the facts discussed by Hudson.¹¹
300 However, if a specific value should be reported for a particular rock type and is needed by analytical or
301 numerical solutions, then intrinsic tensile strength of the rock can be determined following the procedure in this
302 study with the aid of newly developed PM.

303 Brittle nature of rock materials is a major issue for fabricating sharp notch in SCB specimens to successfully
304 determine material fracture toughness. In this study, notch mechanics and practical developments in similar
305 materials were introduced to circumvent this difficulty. From the experimental observations and comparison
306 with different methods, it is being suggested that Gomez et al.²⁵ formula can be used to successfully rectify the
307 notch root radius effect on determining fracture toughness of rock materials. However, if the notch root radius
308 is smaller than the cohesive length, the ISRM suggested method²⁸ is a reliable method for determining fracture

309 toughness of rock materials. Based on the results of this study, the cohesive length is around 1mm for rock
310 materials. Therefore, if the notch width is less than 1mm or notch root radius is less than 500 microns, as
311 specified in the ISRM suggested method,²⁸ then the material fracture toughness measured by this method is
312 reasonably close to the real value.

313 Although, the results are satisfying, there is a mismatch between the actual location and the considered
314 intersection point for estimating the intrinsic tensile strength because of material heterogeneities and theoretical
315 assumptions. This is why fracture toughness values estimated from SCB tests modified for notch root effect and
316 developed PM are a bit different. The question remains open in this study is that how this issue can be rectified
317 and if there is any way to measure L or ℓ_c for different materials to get the best possible results. In other words,
318 the length of the fracture process zone in the direction of crack propagation or the cohesive length ℓ_c should be
319 quantified to determine the actual stress at the tip of cohesive zone right before failure of a material in order to
320 precisely measure the material fracture toughness. Further investigations and future researches are required to
321 exactly quantify the length of fracture process zone and answer this question.

322

323 **Acknowledgements**

324 S. A. wishes to acknowledge the support from Australian Government Research Training Program (RTP)
325 Scholarship and the Monash International Tuition Scholarship (MITS). This research was financially supported
326 by the Australian Research Council (DE200101293), Australian Synchrotron, the MASSIVE HPC facility
327 (www.massive.org.au), and the Monash Centre for Electron Microscopy (MCEM).

328

329 **Declaration of competing interest**

330 The authors would like to declare that there is no conflict of interests regarding publication of this article.

331

332 **Appendix A**

333 Following Taylor,³⁰ derivation of Eq. (2) starts by Westergaard's equation⁴⁷ that provides estimation of
334 tensile stress $\sigma(r)$ in the direction of crack propagation as a function of distance r from the crack tip, for a
335 through-thickness crack of a half-length a in an infinite body. The equation can be read as:

$$\sigma(r) = \sigma \sqrt{\frac{a}{2r}} \quad (\text{A1})$$

336 if $r \ll a$ i.e. for the comparatively close points to the crack tip for an applied tensile stress σ .

337 According to LEFM for the same conditions mode I stress intensity factor K_I can be calculated:

$$K_I = \sigma \sqrt{\pi a} \quad (\text{A2})$$

338 At the moment of failure K_I and σ can be replaced by critical mode one stress intensity factor or fracture
339 toughness K_{Ic} and tensile failure stress σ_f , respectively:

$$K_{Ic} = \sigma_f \sqrt{\pi a} \quad (\text{A3})$$

340 Finally, combining the PM criterion Eq. (1) with Eqs. (A1 and A3), σ_f^2 is equal to both side of the Eq. (A4):

$$\frac{L\sigma_0^2}{a} = \frac{K_{Ic}^2}{\pi a} \quad (\text{A4})$$

341 which is another form of the Eq. (2).

342 Derivation of Eq. (3) can be summarized as follows. If a crack or notch with length a as shown in [Fig. A1](#)
343 is considered, then distribution of $\sigma_c(x, 0)$ along ℓ_c ranged from the physical crack tip or notch tip to fictitious
344 crack tip would be non-linear. The general formula for calculating mode I stress-intensity factor associated with
345 such cohesive stresses K_I^c for a straight crack in an infinite body can be formulated as follows:¹

$$K_I^c = -2\sqrt{(c/\pi)} \int_0^c \frac{\sigma_c(x, 0)}{\sqrt{c^2 - x^2}} dx \quad (\text{A5})$$

346 where $c = a + \ell_c$ and $\sqrt{c^2 - x^2}$ is Green's function. There is no close form solution for this equation since the
347 distribution of σ_c over ℓ_c is unknown. The D–B formula is derived by simplifying this condition. If we consider
348 σ_c over ℓ_c has a constant value (strip model), then Eq. (A5) will transform to:

$$K_I^c = -\sqrt{(2/\pi)} \int_a^c \frac{\sigma_c(x, 0)}{\sqrt{x}} dx \quad (\text{A6})$$

349 **Fig. A2** shows this simplified situation for a crack of length $2(a + \ell_c) = 2c$ in an infinite body under uniaxial
 350 tensile stress σ . Then, using superposition of the problem, and right before crack propagation, the following
 351 equilibrium could be reached:

$$K_I = -K_I^c \quad (\text{A7})$$

352 where K_I is given in Eq. (A2) and K_I^c can be solved using Eq. A6. Now, the equilibrium can be rewritten as
 353 follows:

$$\sigma\sqrt{\pi c} = 2\sigma_c\sqrt{\frac{c}{\pi}}\cos^{-1}\frac{a}{c}; \quad (\text{A8})$$

$$\rightarrow \sqrt{\pi c} \left(\sigma - \frac{2\sigma_c}{\pi} \cos^{-1} \frac{a}{c} \right) = 0;$$

$$\therefore \frac{a}{a + \ell_c} = \cos \left(\frac{\pi\sigma}{2\sigma_c} \right)$$

354 Finally, by two reasonable assumptions including $\ell_c \ll a$ and $\sigma \ll \sigma_c$ this equilibrium can be solved for ℓ_c :

$$1 - \frac{\ell_c}{a} = 1 - \frac{\pi^2\sigma^2}{8\sigma_c^2}; \quad (\text{A9})$$

$$\rightarrow \ell_c = \frac{\pi\sigma^2\pi a}{8\sigma_c^2}$$

355 that is another form of Eq. (3).

356

357 **Appendix B**

358 The iterative method for estimating material fracture toughness K_{Ic} from Gomez et al.²⁵ practical formula
 359 (Eq. 11) can be presented as follows. First of all, Eq. 11 can be divided in the two following formulas:

$$\frac{K_{Ic}^U}{K_{Ic}} = \sqrt{1 + \frac{\pi \rho}{4 l_{ch}}} \quad (B1)$$

360 where l_{ch} is a characteristic length given in Eq. B2:

$$l_{ch} = (K_{Ic}/\sigma_c)^2. \quad (B2)$$

361 Then, an iterative process for estimating K_{Ic} can be presented in four steps as follows:

- 362 a) estimating the l_{ch} using Eq. (B2) by assuming K_{Ic} is equal to the measured generalized fracture
 363 toughness from experiment;
- 364 b) estimating the material fracture toughness by replacing the measured generalized fracture
 365 toughness from experiment, notch tip radius ρ , and the calculated l_{ch} from the first step into Eq.
 366 (B1);
- 367 c) updating the l_{ch} by replacing the estimated material fracture toughness from the second step into
 368 Eq. (B2); and
- 369 d) repeating this loop several times until old and new l_{ch} values and accordingly material fracture
 370 toughness values converge.

371 The larger the ρ or the smaller the l_{ch} , the greater the number of required iterations for convergence (see Fig.
 372 4-a).

373 This method has a limitation that is connected to the ratio of ρ/l_{ch} . Based on some numerical examples, it
 374 turns out that this iterative process works well if ρ is smaller or slightly larger than l_{ch} . It is notable that if $\rho =$
 375 l_{ch} , then $K_{Ic}/K_c^U \approx 0.5$ (after convergence).

376

377 **References**

- 378 1. Lawn B. Fracture of Brittle Solids. London: Cambridge University Press; 1993.
- 379 2. Myer LR, Kemeny JM, Zheng Z, Suarez R, Ewy RT, Cook NGW. Extensile cracking in porous rock under
 380 differential compressive stress. Appl Mech Rev 1992;45(8):263–280.

- 381 3. Haimson BC, Cornet FH. ISRM suggested methods for rock stress estimation—Part 3: hydraulic fracturing
382 (HF) and/or hydraulic testing of pre-existing fractures (HTPF). *Int J Rock Mech Min Sci*. 2003;40:1011–
383 1020.
- 384 4. Weibull W. A statistical distribution function of wide applicability. *J Appl Mech*. 1951;18(3):293–297.
- 385 5. Bazant ZP, Planas J. *Fracture and Size Effect in Concrete and Other Quasibrittle Materials*. Boca Raton
386 Florida: CRC Press; 1997.
- 387 6. Perras M, Diederichs M. A review of the tensile strength of rock: concepts and testing. *Geotech Geol Eng*.
388 2014;32:525–546.
- 389 7. Justo J, Castro J, Cicero S. Application of the Theory of Critical Distances for the Fracture Assessment of a
390 Notched Limestone Subjected to Different Temperatures and Mixed Mode with Predominant Mode I
391 Loading Conditions. *Rock Mech Rock Eng*. 2021; <https://doi.org/10.1007/s00603-021-02365-7>.
- 392 8. Atkinson BK. Subcritical crack growth in geological materials. *J Geophys Res: Solid Earth*.
393 1984;89(B6):4077–4114.
- 394 9. Barenblatt GI. The mathematical theory of equilibrium cracks in brittle fracture. *Adv Appl Mech*. 1962;7:55–
395 129.
- 396 10. Xu XP, Needleman A. Numerical simulations of fast crack growth in brittle solids. *J Mech Phys Solids*.
397 1994;42(9):1397–1434.
- 398 11. Hudson JA. Tensile strength and the ring test. *Int J Rock Mech Min Sci Geomech Abstr*. 1969;6:91–97.
- 399 12. Taylor D. The theory of critical distances. *Eng Fract Mech*. 2008;75:1696–1705.
- 400 13. Ibáñez-Gutiérrez FT, Cicero S, Carrascal IA, Procopio I. Effect of fibre content and notch radius in the
401 fracture behaviour of short glass fibre reinforced polyamide 6: an approach from the Theory of Critical
402 Distances. *Comp Part B: Eng*. 2016; 94:299–311.
- 403 14. Ibáñez-Gutiérrez FT, Cicero S, Carrascal IA. On the influence of moisture content on the fracture behaviour
404 of notched short glass fibre reinforced polyamide 6. *Comp Part B: Eng*. 2019;159:62–71.
- 405 15. Susmel L, Taylor D. Fatigue design in the presence of stress concentrations. *Int J Strain Analy*. 2003;38:443–
406 452.
- 407 16. Susmel L, Taylor D. On the use of the theory of critical distances to predict static failures in ductile
408 metallic materials containing different geometrical features. *Eng Fract Mech*. 2008;75:4410–4421.

- 409 17. Pereira JCR, de Jesus AMP, Xavier J, Correia JAFO, Susmel L, Fernandes AA. Low and ultra-low-cycle
410 fatigue behavior of X52 piping steel based on theory of critical distances. *Int J Fatigue*. 2020;134:1–9.
- 411 18. Cicero S, Torabi AR, Madrazo V, Azizi P. Prediction of fracture loads in PMMA Unnotched specimens using
412 the equivalent material concept and the theory of critical distances combined criterion. *Fatigue Fract Eng*
413 *Mater Struct*. 2017;1–12.
- 414 19. Peron M, Torgersen J, Berto F. A novel approach for assessing the fatigue behavior of PEEK in a
415 physiologically relevant environment. *Materials*. 2018;11:1923.
- 416 20. Cicero S, García T, Castro J, Madrazo V, Andrés D. Analysis of notch effect on the fracture behaviour of
417 granite and limestone: an approach from the theory of critical distances. *Eng Geol*. 2014;177:1–9.
- 418 21. Jenkins A, Fathi E, Belyadi F. Stress field behavior induced by hydraulic fracture in shale reservoirs: a
419 practical view on cluster spacing. *J Nat Gas Sci Eng*. 2017;48:186–196.
- 420 22. Justo J, Castro J, Cicero S, Sánchez-Carro MA, Husillos R. Notch effect on the fracture of several rocks:
421 application of the theory of critical distances. *Theor Appl Fract Mech*. 2017;90:251–258.
- 422 23. Justo J, Castro J, Cicero S. Notch effect and fracture load predictions of rock beams at different temperatures
423 using the theory of critical distances. *Int J Rock Mech Min Sci*. 2020;125:104161.
- 424 24. Creager M, Paris P. Elastic field equations for blunt cracks with reference to stress corrosion cracking. *Int J*
425 *Fract Mech*. 1967;3:247–252.
- 426 25. Gomez FJ, Guinea GV, Elices M. Failure criteria for linear elastic materials with Unotches. *Int J Fract*.
427 2006;141:99–113.
- 428 26. Lazzarin P, Filippi S. A generalized stress intensity factor to be applied to rounded V-shaped notches. *Int J*
429 *Solids Struct*. 2006;43:2461–2478.
- 430 27. Tanné E, Li T, Bourdin B, Marigo JJ, Maurini C. Crack nucleation in variational phase-field models of
431 brittle fracture. *J Mech Phys Solids*. 2018;110:80–99.
- 432 28. Kuruppu MD, Obara Y, Ayatollahi MR, Chong KP, Funatsu T. ISRM-suggested method for determining
433 the Mode I static fracture toughness using semi-circular bend specimen. *Rock Mech Rock Eng*.
434 2014;47(1):267–274.
- 435 29. Taylor D. Predicting the fracture strength of ceramic materials using the theory of critical distances. *Eng*
436 *Fract Mech*. 2004;71:2407–2416.

- 437 30. Taylor D. *The Theory of Critical Distances: A New Perspective in Fracture Mechanics*. Oxford, UK:
438 Elsevier; 2007.
- 439 31. Dugdale DS. Yielding of steel sheets containing slits. *J Mech Phys Solids*. 1960;8:100–104.
- 440 32. Hobbs DW. An assessment of a technique for determining the tensile strength of rock. *Br J Appl Phys*.
441 1965;16:259–268.
- 442 33. Zhang XJ, Yi YN, Zhu HB, Liu GY, Sun LB, Shi L, Jiang H, Ma SP. Measurement of tensile strength of
443 nuclear graphite based on ring compression test. *J Nucl Mater*. 2018;511:134–140.
- 444 34. Bai QS, Tu SH, Zhang C. DEM investigation of the fracture mechanism of rock disc containing hole(s) and
445 its influence on tensile strength. *Theor Appl Fract Mec*. 2016;86:197–216.
- 446 35. Filon LNG. The stresses in a circular ring. *Sel Engng Pap Instn Civ Engrs*. 1924;Paper No. 12.
- 447 36. Torabi AR, Etesam S, Sapora A, Cornetti P. Size effects on brittle fracture of Brazilian disk samples
448 containing a circular hole. *Eng Fract Mech*. 2017;496–503.
- 449 37. ISRM. The complete ISRM suggested methods for rock characterization, testing and monitoring: 1974–
450 2006. In: R. Ulusay, J.A. Hudson (eds) *Suggested methods prepared by the commission on testing methods*,
451 *International Society for Rock Mechanics*, compilation arranged by the ISRM Turkish National Group.
452 Kozan Ofset, Ankara: 2007.
- 453 38. Nara Y, Kaneko K. Study of subcritical crack growth in andesite using the Double Torsion test. *Int J Rock*
454 *Mech Min Sci*. 2005;42:521-530.
- 455 39. Ponson L. Depinning transition in the failure of inhomogeneous brittle materials. *Phys Rev Lett*.
456 2009;103:055501.
- 457 40. Chong KP, Kuruppu MD, New specimen for fracture toughness determination for rock and other materials.
458 *Int J Fract*. 1984; 26(2):R59–R62.
- 459 41. Aliha MRM, Hosseinpour GR, Ayatollahi MR. Application of cracked triangular specimen subjected to
460 three-point bending for investigating fracture behavior of rock materials. *Rock Mech Rock Eng*.
461 2013;46(5):1023–1034.
- 462 42. Zhang QB, Zhao J. Effect of loading rate on fracture toughness and failure micromechanisms in marble.
463 *Eng Fract Mech*. 2013;102:288–309.

- 464 43. Nejati M, Aminzadeh A, Driesner T, Saar MO. On the directional dependency of Mode I fracture toughness
465 in anisotropic rocks. *Theor Appl Fract Mech.* 2020;107:102494.
- 466 44. Li D, Wong LNY. The Brazilian disc test for rock Mechanics applications: review and new insights. *Rock*
467 *Mech Rock Eng.* 2013;46(2):269–287.
- 468 45. Peterson RE. Notch-sensitivity. In *Metal Fatigue* (Edited by Sines G and Waisman JL.). New York: McGraw
469 Hill; 1959;293–306.
- 470 46. Gross D, Seelig T. *Fracture Mechanics With an Introduction to Micromechanics*, Third ed. Berlin: Springer-
471 Verlag; 2018.
- 472 47. Westergaard HM. Bearing Pressures and Cracks, *J Appl Mech.* 1939;6:49–53.

473 **List of Figures**

474 Fig. 1. Ring experiment: (a) Schematic of the ring specimen; (b) A marble ring with an inner radius of 15mm
475 under compression; and (c) Specimens with the minimum inner radii before testing.

476 Fig. 2. a) Sandstone ring specimen under compression; b) Mechanical response of the sandstone ring specimens
477 with different inner radii; c) Schematic illustration of the two steps failure behaviour of ring specimens; and d)
478 Mechanical response of the ring specimens made of different rocks for the largest inner radii (13-15mm).

479 Fig. 3. Sequence of high-speed images taken from a sandstone ring with an inner radius of 3 mm showing
480 symmetric fracture propagation from point A, as depicted in Fig. 2-c.

481 Fig. 4. SCB fracture tests: (a) Schematic of SCB specimen under three point bending; (b) Schematic of the stress
482 distribution on the bisector line of a blunted notch under opening mode loading conditions; (c) SCB specimens
483 before testing; and (d) 2D image slice of a sandstone SCB specimen scanned by means of X-ray tomography
484 after failure. Note the radius $\rho \approx 350\mu\text{m}$ of the initial notch.

485 Fig. 5. (a) Sequence of high-speed images taken from a fine-grained granite SCB specimen showing crack
486 initiation and growth from the initial notch tip; (b) Mechanical response of the notched SCB specimens for the
487 four rocks investigated.

488 Fig. 6. Graphical guides for modifying the notch root radius effect on material fracture toughness: a) A 3D guide
489 showing the iterative process; and b) A guide for estimating K_{Ic} as a function of notch tip radius, intrinsic tensile
490 strength and generalized fracture toughness. c) K_{Ic} as a function of notch tip radius, the cohesive length and
491 generalized fracture toughness; and d) a single master curve for evaluating K_{Ic} as a function of ℓ_c/ρ ratio and
492 generalized fracture toughness.

493 Fig. 7. Failure load P_{max} (a) and apparent tensile strength σ_{max} (b) of the different rocks investigated as obtained
494 from the different fracture tests.

495 Fig. 8. Application of the PM for the determination of the tensile strength: Stress distribution against distance
496 for the two geometries displaying the highest and the lowest stress concentrations for (a) sandstone, (b) marble,
497 (c) fine-grained granite and (d) coarse-grained granite. The point of intersection of both curves provide the
498 intrinsic tensile strength as well as the cohesive length, as illustrated for marble in the panel (b).

499 Fig. 9. Tensile Stress distribution against distance at the onset of failure for different fracture test geometries
500 and different materials: a) sandstone; b) marble; c) fine-grained granite; and d) coarse-grained granite.

501 Fig. A1. Schematic of Barenblat cohesive zone model

502 Fig. A2. Equilibrium for derivation of D–B formula as superposition of applied and cohesive stresses

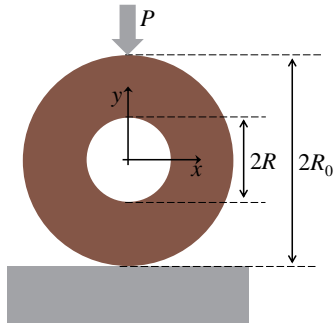
503 **List of Tables**

504 Table 1. The intrinsic tensile strength, the cohesive half-length and the material fracture toughness, determined
505 by the developed PM.

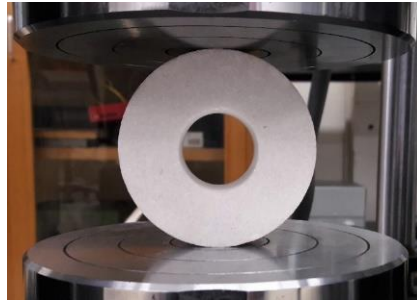
506 Table 2. Comparison of measured generalized fracture toughness K_{Ic}^U [MPa.m^{0.5}] and modified fracture
507 toughness K_{Ic} [MPa.m^{0.5}] values with those obtained using the common and developed PMs.

508 Table 3. The cohesive length ℓ_c [mm] as per D–B formula determined both from SCB tests modified for the
509 rounded notch tip effect and the developed PM.

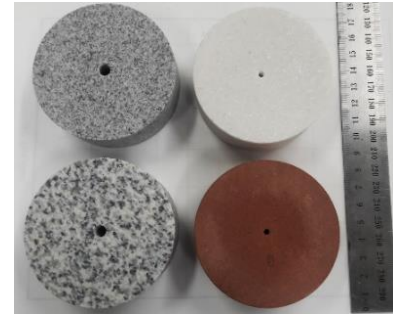
510



(a)



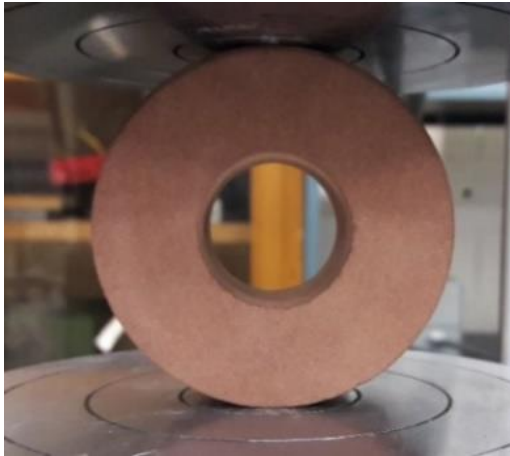
(b)



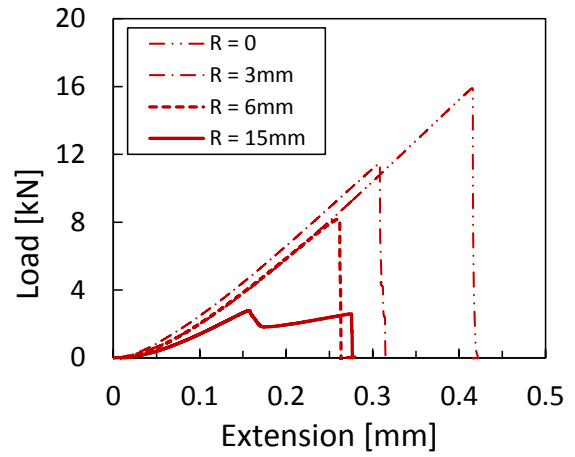
(c)

511 Fig. 1. Ring experiment: (a) Schematic of the ring specimen; (b) A marble ring with an inner radius of 15mm
512 under compression; and (c) Specimens with the minimum inner radii before testing.

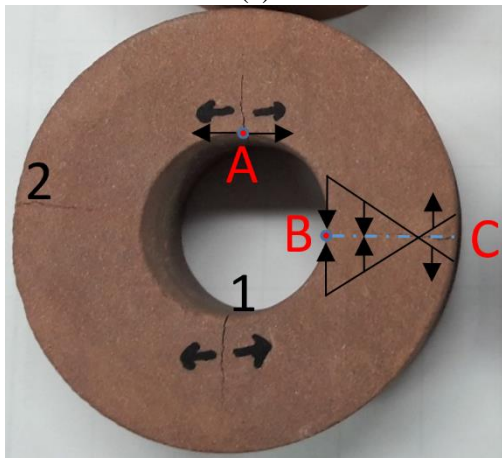
513



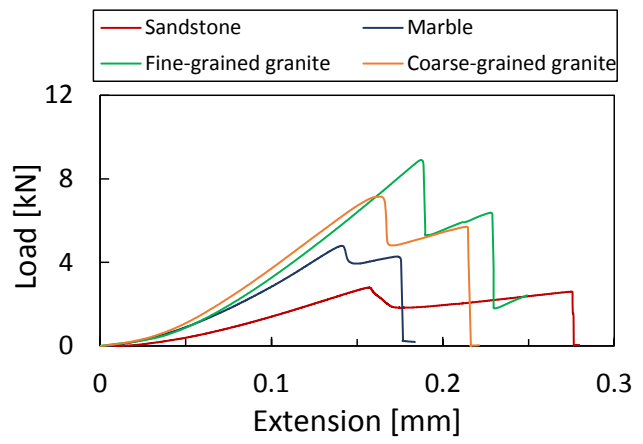
(a)



(b)



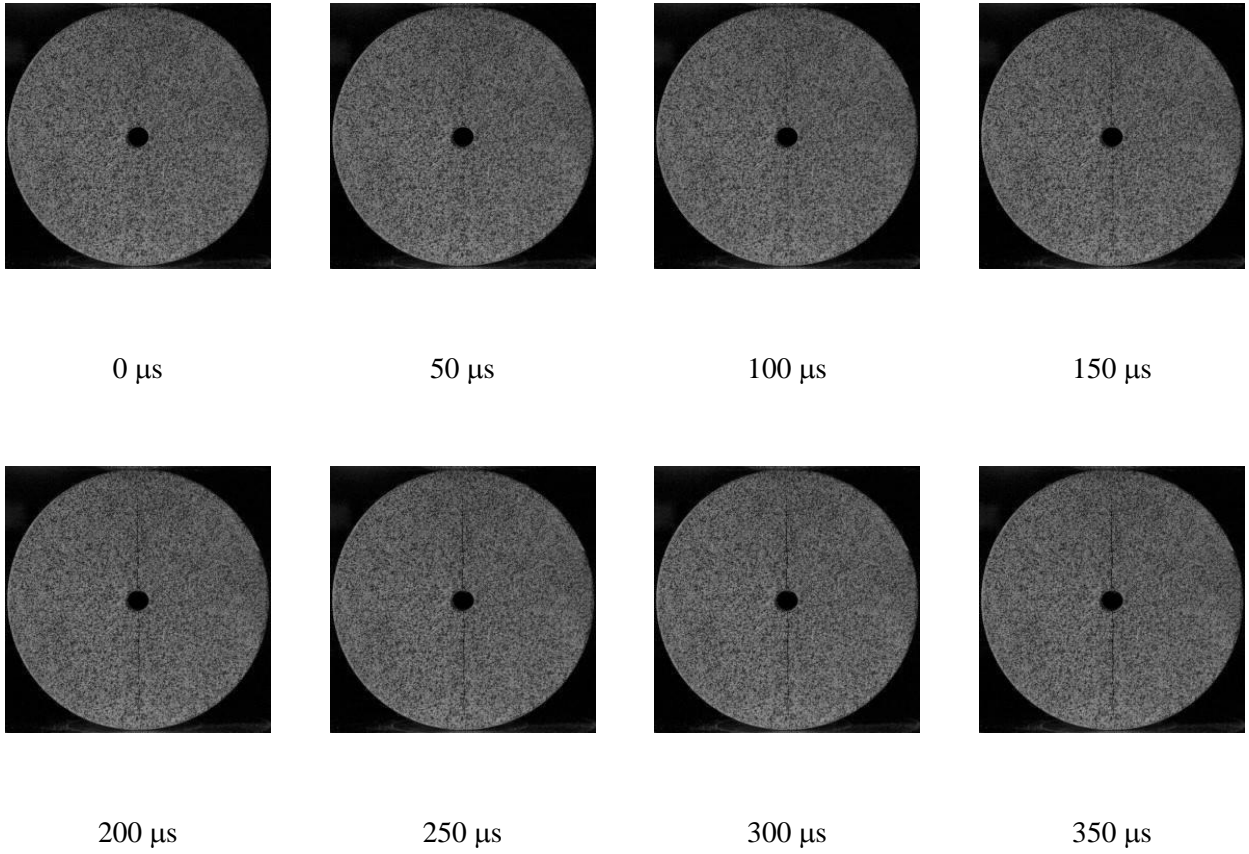
(c)



(d)

514 Fig. 2. a) Sandstone ring specimen under compression; b) Mechanical response of the sandstone ring specimens
 515 with different inner radii; c) Schematic illustration of the two steps failure behaviour of ring specimens; and d)
 516 Mechanical response of the ring specimens made of different rocks for the largest inner radii (13-15mm).

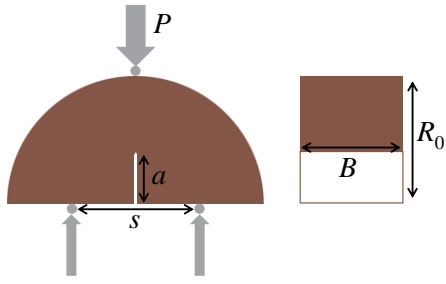
517



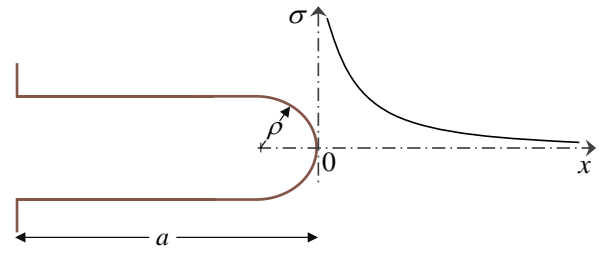
518 Fig. 3. Sequence of high-speed images taken from a sandstone ring with an inner radius of 3 mm showing
519 symmetric fracture propagation from point A, as depicted in Fig. 2-c.

520

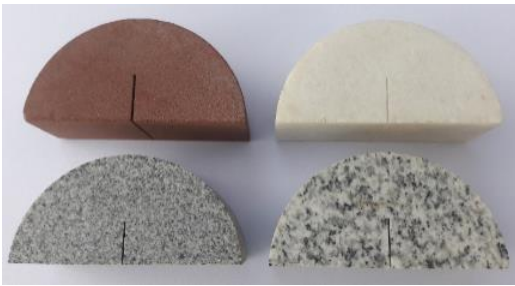
521



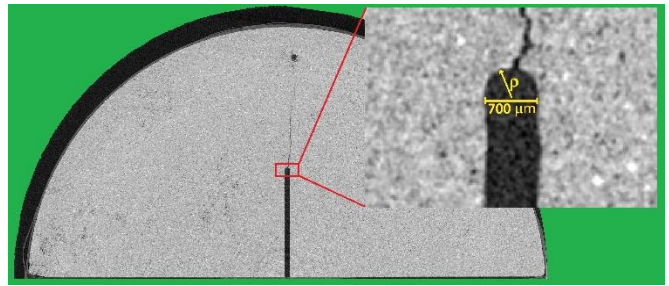
(a)



(b)



(c)

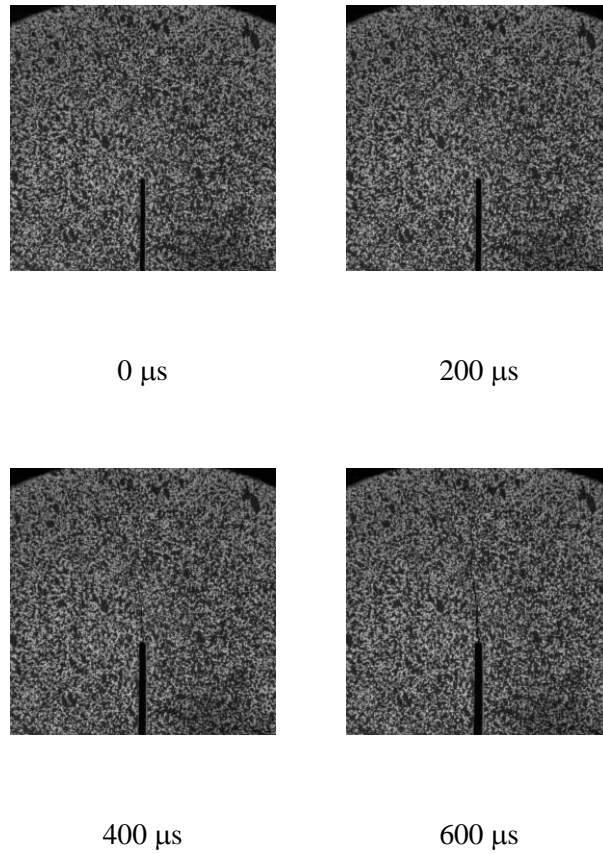


(d)

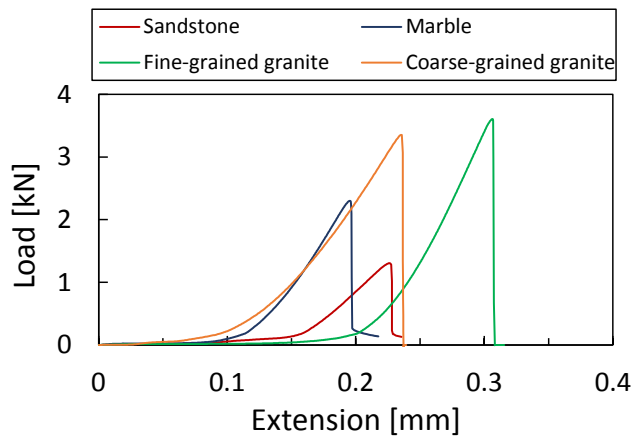
522 Fig. 4. SCB fracture tests: (a) Schematic of SCB specimen under three point bending; (b) Schematic of the stress
 523 distribution on the bisector line of a blunted notch under opening mode loading conditions; (c) SCB specimens
 524 before testing; and (d) 2D image slice of a sandstone SCB specimen scanned by means of X-ray tomography
 525 after failure. Note the radius $\rho \approx 350\mu\text{m}$ of the initial notch.

526

527

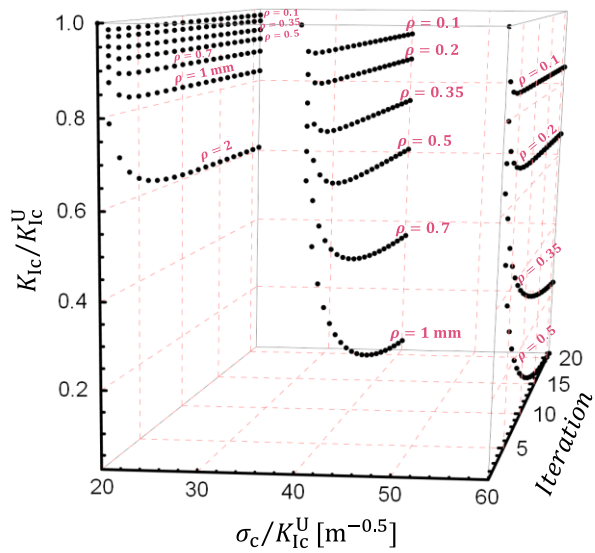


(a)

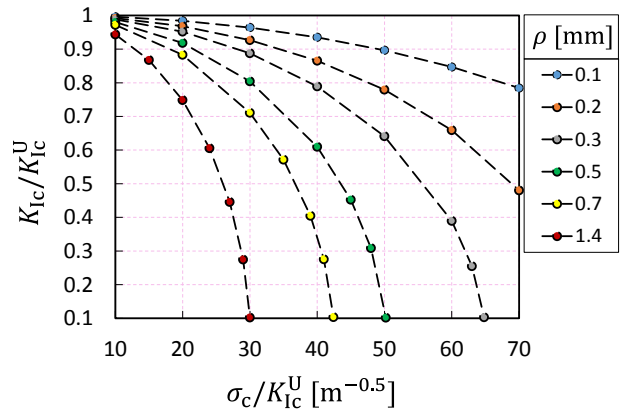


(b)

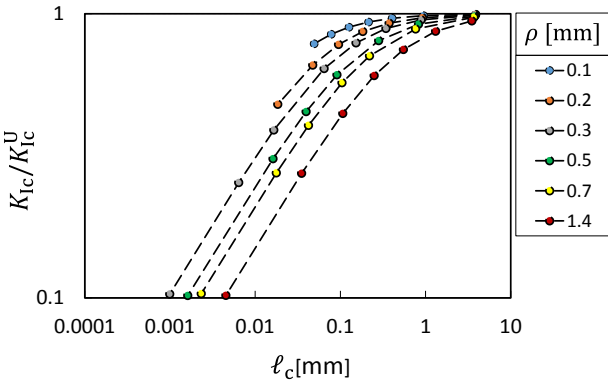
528 Fig. 5. (a) Sequence of high-speed images taken from a fine-grained granite SCB specimen showing crack
 529 initiation and growth from the initial notch tip; (b) Mechanical response of the notched SCB specimens for the
 530 four rocks investigated.



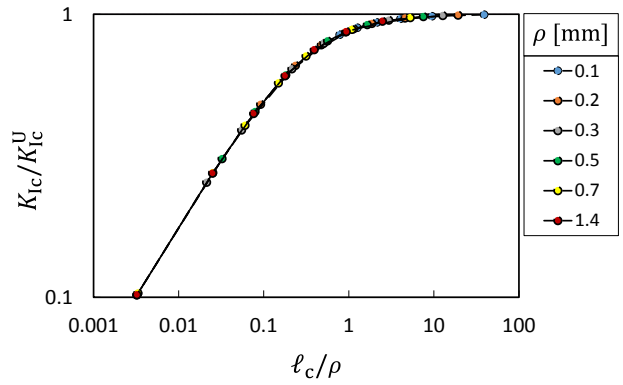
(a)



(b)



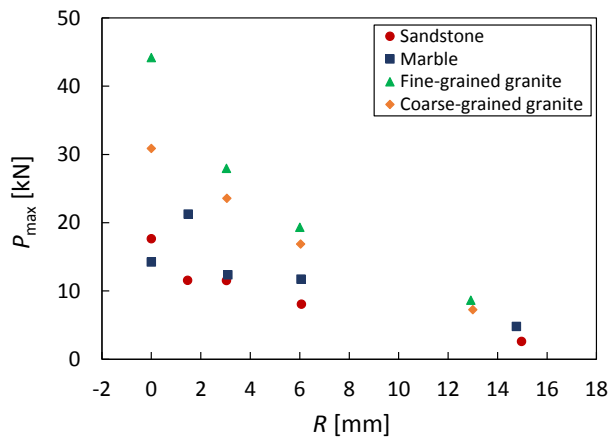
(c)



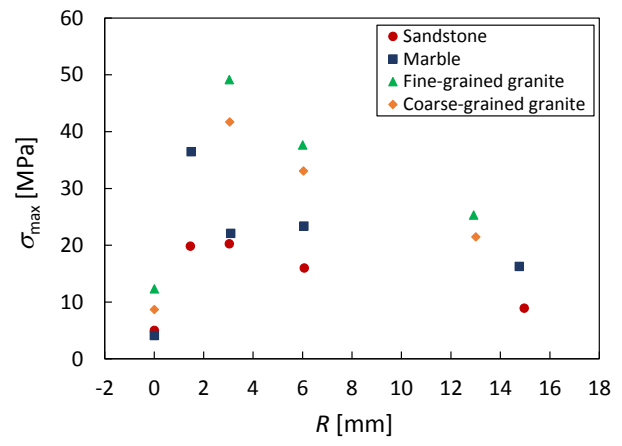
(d)

531 Fig. 6. Graphical guides for modifying the notch root radius effect on material fracture toughness: a) A 3D guide
 532 showing the iterative process; and b) A guide for estimating K_{Ic} as a function of notch tip radius, intrinsic tensile
 533 strength and generalized fracture toughness. c) K_{Ic} as a function of notch tip radius, the cohesive length and
 534 generalized fracture toughness; and d) A single master curve for evaluating K_{Ic} as a function of l_c/ρ ratio and
 535 generalized fracture toughness.

536



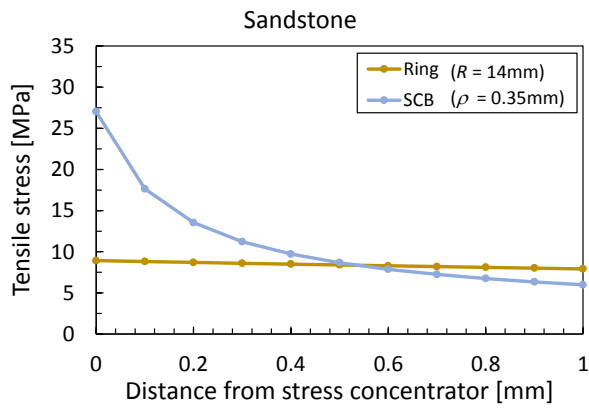
(a)



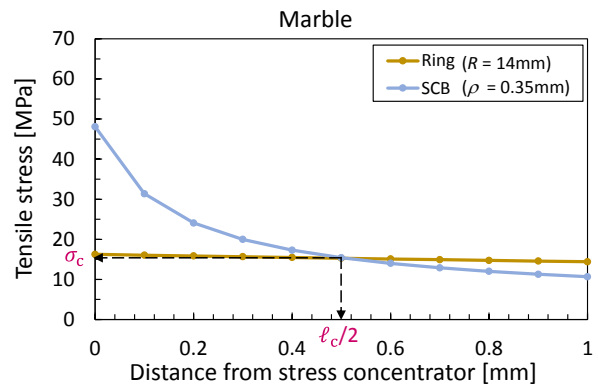
(b)

537 Fig. 7. Failure load P_{\max} (a) and apparent tensile strength σ_{\max} (b) of the different rocks investigated as obtained
 538 from the different fracture tests.

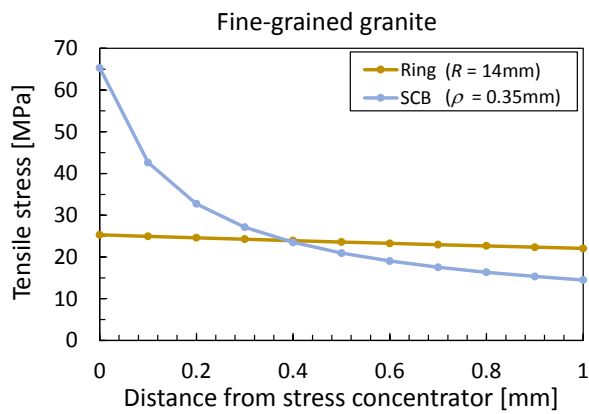
539



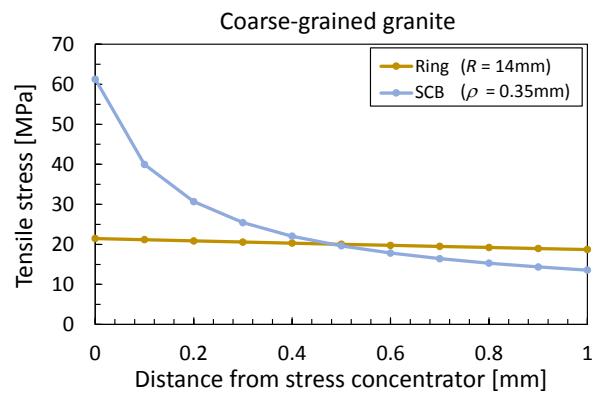
(a)



(b)



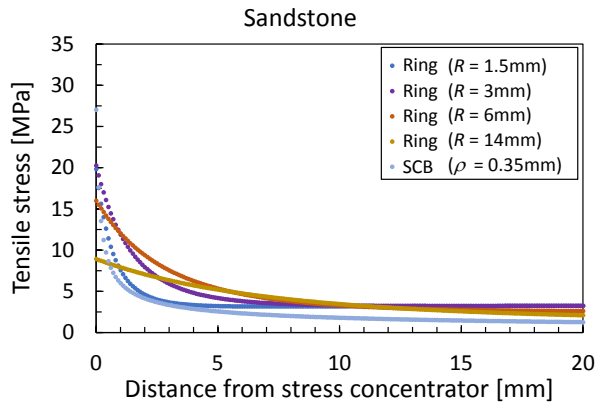
(c)



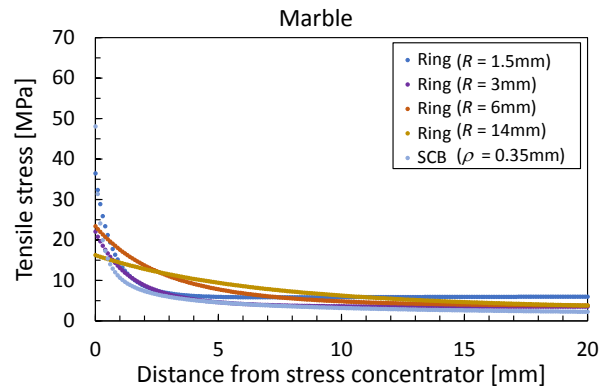
(d)

540 Fig. 8. Application of the PM for the determination of the tensile strength: Stress distribution against distance
 541 for the two geometries displaying the highest and the lowest stress concentrations for (a) sandstone, (b) marble,
 542 (c) fine-grained granite and (d) coarse-grained granite. The point of intersection of both curves provide the
 543 intrinsic tensile strength as well as the cohesive length, as illustrated for marble in the panel (b).

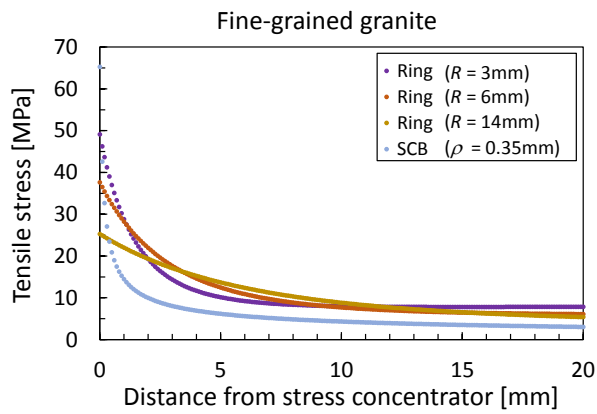
544



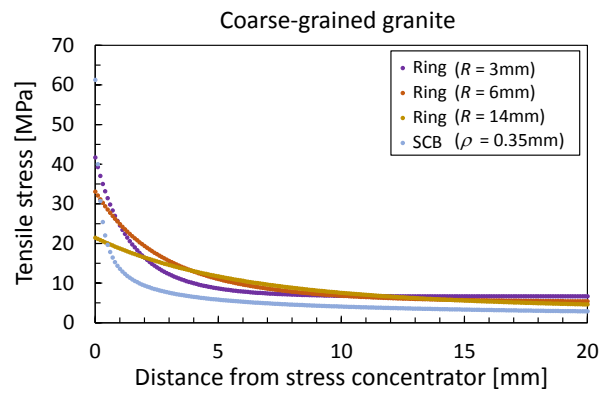
(a)



(b)



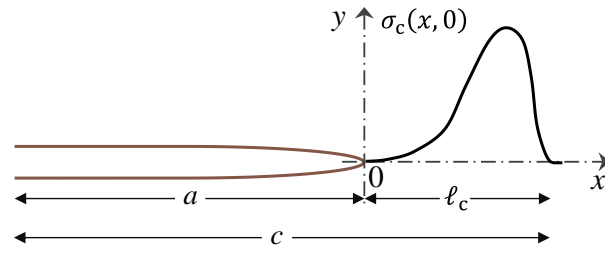
(c)



(d)

545 Fig. 9. Tensile Stress distribution against distance at the onset of failure for different fracture test geometries
 546 and different materials: a) sandstone; b) marble; c) fine-grained granite; and d) coarse-grained granite.

547

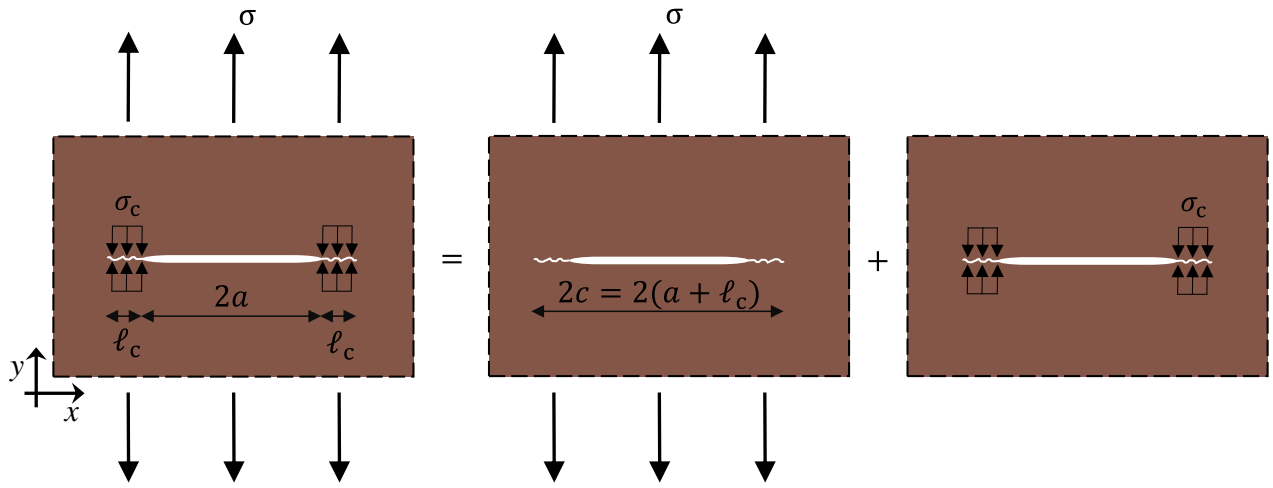


548

549

Fig. A1. Schematic of Barenblatt cohesive zone model.

550



551

552 Fig. A2. Equilibrium for derivation of D-B formula as superposition of applied tensile and cohesive stresses.

553

554 Table 1. The intrinsic tensile strength, the cohesive half-length and the material fracture toughness, determined
555 by the developed PM.

Rock type	σ_c [MPa]	$l_c/2$ [mm]	K_{Ic} [MPa.m ^{0.5}]
Sandstone	8.4	0.53	0.44
Marble	15.4	0.51	0.78
Fine grained granite	24.0	0.39	1.07
Coarse grained granite	19.8	0.48	0.98

556

557

558 Table 2. Comparison of measured generalized fracture toughness K_{Ic}^U [MPa.m^{0.5}] and modified fracture
 559 toughness K_{Ic} [MPa.m^{0.5}] values with those obtained using the common and developed PMs.

Rock type	K_{Ic}^U (ISRM ²⁸)	K_{Ic} (Gomez et al. ²⁵)	K_{Ic} (common PM)	K_{Ic} (developed PM)
Sandstone	0.45	0.43	0.49	0.44
Marble	0.80	0.76	0.86	0.78
Fine grained granite	1.08	1.00	1.19	1.07
Coarse grained granite	1.02	0.97	1.11	0.98

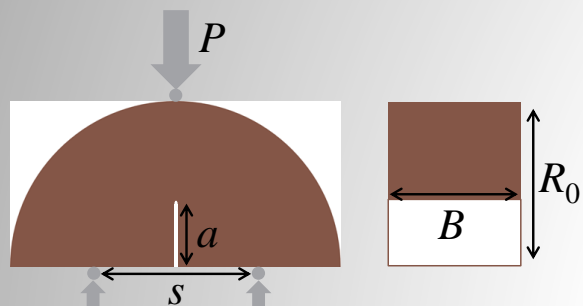
560

561 Table 3. The cohesive length ℓ_c [mm] as per D–B formula determined both from SCB tests modified for the
562 rounded notch tip effect and the developed PM.

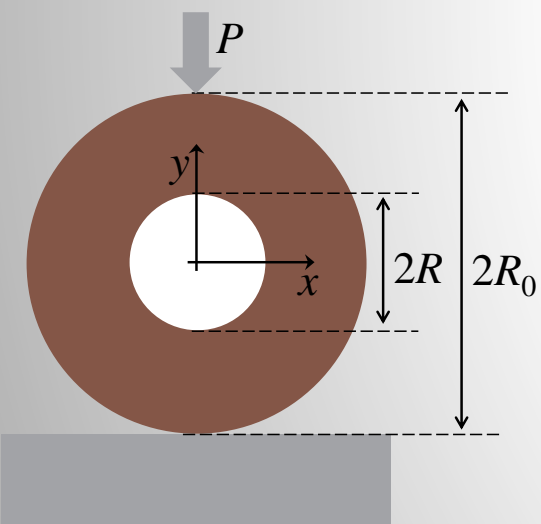
Rock type	Experimental	Developed PM
Sandstone	1.03	1.07
Marble	0.96	1.01
Fine grained granite	0.68	0.78
Coarse grained granite	0.94	0.96

563

Performing experiments



SCB test: High stress concentration



Ring test: Low stress concentration



Applying Point Method

SCB test:

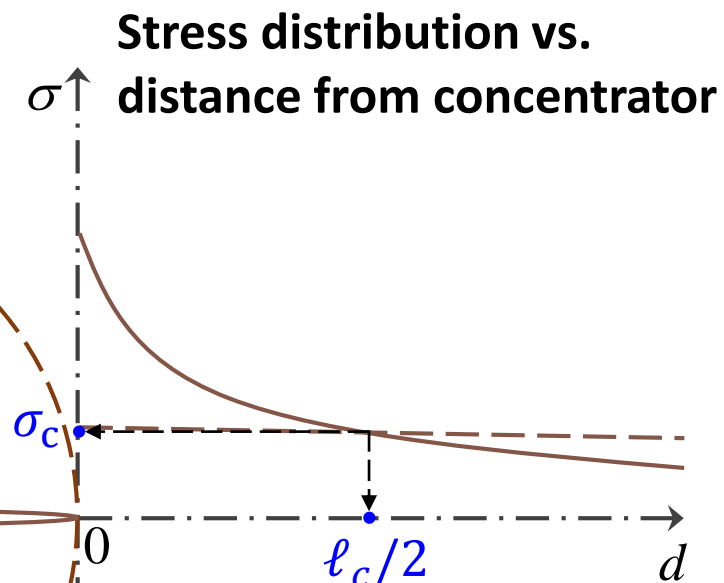
$$\sigma(d, 0) = \frac{2K_{Ic}^U}{\sqrt{\pi}} \frac{d + \rho}{(2d + \rho)^{3/2}}$$

Creager-Paris solution

Ring test:

$$\sigma(d, 0) = \frac{\sigma_{max}}{2} \left(2 - 2 \frac{R^2}{d^2} + 12 \frac{R^4}{d^4} \right) \left(1 + \frac{19}{3} \left(\frac{R}{R_0} \right)^2 \right)$$

Kirsch's solution and Hobbs' correction



Modifying PM

$$\sigma(\ell_c/2) = \sigma_c$$



Estimating fracture toughness

$$K_{Ic} = f(\ell_c, \sigma_c)$$



Validating the results

$$K_{Ic}(\text{Experimental}) \approx K_{Ic}(\text{Developed PM})$$